RESEARCH ARTICLE
SPACE PHYSICS: IONOSPHERIC PHYSICS

Earth and Planetary Physics
9: 966–979, 2025
doi: 10.26464/epp2025048

Occurrence of ionospheric scintillation during geomagnetic storms in Indonesia (2003–2024) using superposed epoch analysis

Angga Yolanda Putra[1,2], Theodosius Marwan Irnaka[1], Prayitno Abadi[3,4], La Ode Muhammad Musafar Kilowasid[5], Fitri Nuraeni[5], Erlansyah[5], Suraina[1,5], and Afif Rakhman[1*]

[1]Department of Physics, Faculty of Mathematics and Natural Sciences, Universitas Gadjah Mada (UGM), Yogyakarta, Indonesia;

[2]Directorate of Laboratory Management, Research Facilities, and Science and Technology Park, National Research and Innovation Agency (BRIN), Pontianak, Indonesia;

[3]Research Center for Climate and Atmosphere, National Research and Innovation Agency (BRIN), Bandung, Indonesia;

[4]School of Electrical Engineering, Telkom University, Kab. Bandung, Indonesia;

[5]Research Center for Space, National Research and Innovation Agency (BRIN), Bandung, Indonesia

Key Points:

- The local time of minimum SYM-*H* significantly affects the post-sunset ionospheric scintillation formation during geomagnetic storms.
- Post-sunset ionospheric scintillation occurs about 6 hours after minimum SYM-*H* in weak-moderate geomagnetic storms, and 12 hours in strong storms.
- The disturbance dynamo electric field lasts at least 6 hours in weak-moderate and 12 hours in strong geomagnetic storms.

Citation: Putra, A. Y., Irnaka, T. M., Abadi, P., Kilowasid, L. O. M. M., Nuraeni, F., Erlansyah, Suraina, Rakhman, A. (2025). Occurrence of ionospheric scintillation during geomagnetic storms in Indonesia (2003–2024) using superposed epoch analysis. *Earth Planet. Phys.*, *9*(4), 966–979. http://doi.org/10.26464/epp2025048

Abstract: Ionospheric scintillation refers to rapid radio signal amplitude and phase fluctuations due to small-scale irregularities in the ionosphere. Occurring primarily at equatorial and low latitudes, scintillation is linked to equatorial plasma bubbles (EPBs), regions of depleted plasma density that form after sunset. Ionospheric scintillation typically occurs from post-sunset hours until midnight. Post-sunset EPBs can be enhanced or suppressed during geomagnetic storms, depending on local sunset timing and how it relates to the storm's main or recovery phases. This study analyzes ionospheric scintillation in Indonesia, located at low geomagnetic and geographic latitudes, during geomagnetic events from 2003 to 2024. Using the S4 index, scintillation was examined with data from seven observation stations during geomagnetic storm events. Geomagnetic activity was evaluated using *Dst*, SYM-*H*, and *AE* indices, employing Superposed Epoch Analysis (SEA) to assess scintillation occurrence linked to minimum SYM-*H*, defined as epoch 0 to represent the storm peak or the onset of recovery phase in each event. The analysis categorized geomagnetic storms into weak-moderate (–100 nT < min. *Dst* ≤ –30 nT) and strong (min. *Dst* ≤ –100 nT), and examined their dependence on the local time of minimum SYM-*H*. Results indicate that scintillation first appears ~6 hours after epoch 0 in weak-moderate geomagnetic storms, and ~12 hours after epoch 0 in strong geomagnetic storms. The average *AE* index returns to its baseline value (quiet condition) ~6 and ~12 hours after epoch 0 for weak-moderate and strong geomagnetic storms, respectively. Further analysis based on the classification of the local time of epoch 0 shows that scintillation occurrence is not observed in post-sunset hours when epoch 0 falls between 16:00 and 19:00 LT for weak-moderate geomagnetic storms. In strong geomagnetic storms, scintillation occurrence during post-sunset hours is absent when epoch 0 is between 10:00 and 19:00 LT. Notably, when the minimum SYM-*H* (epoch 0) nearly coincides with local sunset, scintillation activity occurs around sunset in both weak-moderate and strong geomagnetic storms. Furthermore, when epoch 0 falls within midnight until early morning, scintillation can be generated in the post-sunset hours before epoch 0. Still, post-midnight scintillation is not observed in the equatorial region during the recovery phase of either weak-moderate and strong storm events. Our findings show that when sunset falls before or coincide with epoch 0, the likelihood of post-sunset EPB and scintillation increases, due to the prompt-penetration electric field (PPEF) in the main phase of storm. The disturbance dynamo electric field (DDEF) in the recovery phase driven by equatorward winds from auroral Joule heating operates for at least 6- and 12-hours post-epoch 0 in the cases of weak-moderate and strong geomagnetic storms, respectively. When the local sunset falls within these operational DDEF periods, post-sunset EPBs will likely be suppressed, inhibiting ionospheric scintillation during post-sunset hours. Finally, this study provides essential information for developing more accurate ionospheric scintillation prediction models in space weather services in equatorial regions.

Keywords: geomagnetic storm; ionospheric scintillation; superposed epoch analysis; *AE* index; local time of minimum SYM-*H*; DDEF

First author: A. Y. Putra, angg032@brin.go.id
Correspondence to: A. Rakhman, afif_rakhman@mail.ugm.ac.id
Received 12 DEC 2024; Accepted 12 MAR 2025.
First Published online 30 MAY 2025.

1. Introduction

The phenomenon of ionospheric scintillation in the magnetic equator and low-latitude regions is caused by electron density irregularities in the F-layer of the ionosphere, primarily associated with equatorial plasma bubbles (EPBs). The EPBs form due to the Rayleigh–Taylor Instability (RTI) after sunset, when an enhancement in the eastward electric field, known as pre-reversal enhancement (PRE), strengthens the $\boldsymbol{E} \times \boldsymbol{B}$ upward drift and increases RTI growth rates at higher altitudes (Farley et al., 1970; Kelley, 2009). The electron density irregularities at smaller spatial scales (a few hundred meters) within EPBs cause rapid fluctuations in radio wave amplitude and phase, disrupting the L-band (GHz frequencies) used in satellite-based technologies, such as the Global Navigation Satellite System (GNSS), Synthetic Aperture Radar (SAR), and radio communications (Doherty et al., 2004; Kintner et al., 2007; Roy et al., 2013). Typically, the EPB produces ionospheric scintillation during post-sunset hours, emerging after E-region sunset (approximately 19 LT) and fading around midnight (Abadi et al., 2024). Since the amplitude of ionospheric scintillation depends on the background electron density in the ionosphere, the low-latitude ionospheric scintillation occurrences mostly concentrate at the Equatorial Ionization Anomaly (EIA) region, where electron density is highest (Abadi et al., 2014).

During geomagnetic storms, EPBs form differently than they do in quiet conditions, including in their onset and structures. Geomagnetic storms can induce a global electric field in the ionosphere, which influence the generation and evolution of EPBs. These disturbances are driven by various electrodynamic mechanisms, including under-shielding prompt-penetration electric fields (PPEF), which enhance the eastward electric field in the dusk sector, increasing the $\boldsymbol{E} \times \boldsymbol{B}$ upward drift and triggering strong EPBs formation (Fejer et al., 1999). Studies indicate that stronger storm-driven electric fields often trigger post-sunset super EPBs during the main phase of geomagnetic storms (Ma GY and Maruyama, 2006; Cherniak and Zakharenkova, 2016; Aa et al., 2018; Li G et al., 2018). The latitudinal structure of super EPBs can grow quickly and extend into mid-latitude regions, which differs from the structure of normal EPBs (Sun WJ et al., 2024a). Additionally, super EPBs can generate ionospheric scintillation in mid-latitude areas (Li G et al., 2009), whereas normal occurrences of ionospheric scintillation are typically limited to low-latitude regions (Abadi et al., 2014). During the recovery phase, over-shielding penetration electric fields and disturbance dynamo electric fields (DDEF) may either suppress or enhance EPB formation, depending on the local time of the storm's onset recovery phase and pre-existing ionospheric conditions (De La Beaujardière et al., 2009). Several studies indicate that over-shielding and DDEF can delay the onset of EPBs and scintillation. Li G et al. (2009) found that DDEF can delay the onset of EPB formation in equatorial regions. Furthermore, observations from the recent G5 geomagnetic storm in May 2024 showed that EPB plasma bubbles at equatorial latitudes in Southeast Asia experienced a delayed onset, occurring not in post-sunset hours, but instead appearing at post-midnight, likely due to disturbance dynamo effects (Sun WJ et al., 2024b; Abadi et al., 2025).

While the geomagnetic storm is a global phenomenon, its effects on the generation and suppression of EPBs at specific longitudes depend on the local time of main and recovery phases of the storm. Focusing on East and Southeast Asia, some previous studies on EPBs development during geomagnetic storms have been performed based on case studies and statistical analyses. Spogli et al. (2016) observed that the 2015 St. Patrick's geomagnetic storm significantly suppressed post-sunset EPB and scintillation in Southeast Asia, due to the local sunset in this region not aligning with the main phase of the storm. In contrast, Ram et al. (2016) found that the super EPB occurs in the Indian sector because its local sunset coincides with the main phase of the St. Patrick's storm. These two studies highlight the significantly enhanced equatorial zonal electric field, uniquely confined to the dusk sector, in response to PPEF. Marlia et al. (2019) demonstrated that geomagnetic storm-induced electric field disturbances significantly impact ionospheric scintillation in Southeast Asia, with effects varying based on local time and storm phase. Han et al. (2024) found that storm-driven electric fields can accelerate vertical F-layer drift, enhance RTI growth rates, and trigger plasma bubbles outside of their typical seasonal patterns of occurrence. Putra et al. (2023) reported that ionospheric scintillation over Indonesia increased ~12 hours after the storm peak, suggesting that the heightened auroral activity during the storm influences the delayed scintillation response.

The duration of the effects of the geomagnetic storm on EPB generation motivates the study of the relationship between storm impacts and dynamics in the equatorial ionosphere. Specifically, the influence of storms on ionospheric scintillation generation remains an unresolved question. For example, Shang SP et al. (2008) examined GNSS scintillation in Hainan (19.5°N, 109.1°E), China from 2003 to 2005, demonstrating that geomagnetic storms significantly affect the variation in onset times of scintillations, depending on the timing of the storm's main and recovery phases. Additionally, EPB and scintillation are fundamentally different; EPB refers to a large-scale electron density depletion (> 100 km) that can persist longer in the ionosphere, while scintillation reflects the presence of smaller-scale irregularities that decay faster than the EPB itself. The amplitude of scintillation depends on the background density in the ionosphere. Due to the storm-induced electric field, the EPB can be generated post-midnight when background density is low, and the EPB can even survive after sunrise. But can equatorial scintillation be observed as well? Additionally, this raises the scientific question: when is equatorial ionospheric scintillation generated or inhibited during a geomagnetic storm?

This study aims to reveal the generation and inhibition of ionospheric scintillation in the equatorial region during geomagnetic storms. We analyzed ionospheric scintillation using the S4 index, based on GNSS receiver data from seven stations in Indonesia during geomagnetic storms from 2003 to 2024. We seek to determine when scintillation is generated or inhibited according to the local time of the main and recovery phases of the storm.

The ultimate goal of this study is to support space weather services in Indonesia. As reliance on satellite-based communication and navigation increases, understanding the effects of space weather has become a global priority. Since the International Heliophysical Year (IHY) in 2009, awareness about the impact of space weather on ground-based and satellite infrastructure has grown significantly. In response, Indonesia has strengthened its space weather monitoring efforts, mainly through the national space weather program initiated in 2015, which aims to mitigate the effects of ionospheric scintillation on critical technological systems.

2. Data and Methods

2.1 Space Weather Data

Ionospheric behavior varies in response to changes in space weather, which are influenced by fluctuations in solar wind and its manifestation in Earth's magnetospheric environment (Basavaiah, 2011). Extreme space weather conditions occur during geomagnetic storms, which are marked by the growth of the ring current in the magnetosphere/ionosphere (Burton et al., 1975). This disturbance can be quantified using the *Dst* index, which provides an overview of magnetic field changes with a resolution of 1 hour. The minimum *Dst* is used as a reference for the strength of geomagnetic storms (Loewe and Prolss, 1997). The SYM-*H* index provides a more detailed view of ring current variations, with a 1-minute data resolution. Meanwhile, auroral storms occur at high latitudes through the penetration of electric fields and the injection of particles into Earth's night-side, followed by the growth of partial ring currents. This partial ring current growth can be quantified using the *AE* index (Weygand et al., 2014; Bergin et al., 2020). The *Dst*, SYM-*H*, and *AE* indices are derived from surface magnetometer observation data for the *H* component, representing the north–south magnetic field component. Magnetic activity at equatorial and low latitudes is represented by the *Dst* index, while the SYM-*H* index is calculated from average measurements at mid-latitudes. For auroral latitude regions, magnetic activity is represented by the *AE* index (Davis and Sugiura, 1966; Weygand et al., 2014). These three geomagnetic indices are publicly available through the WDC Kyoto website to support global space weather research (World Data Center for Geomagnetism et al., 2015a, 2015b, 2022).

The interplanetary electric field carried by the solar wind plays an important role in the Sun–Earth interaction. The dawn–dusk component of the interplanetary electric field (E_y) significantly contributes to changes in the ionosphere, where the enhancement of this component influences the Earth's ionospheric dimensions and structure (Manoj et al., 2008; Kikuchi and Hashimoto, 2016), leading to increased electron density (Astafyeva et al., 2016; Imtiaz et al., 2020). This in turn can alter ionospheric characteristics, affecting radio wave propagation and satellite-based communication systems (Doherty et al., 2004; Kintner et al., 2007; Morton et al., 2020). The PPEF phenomenon occurs when the Interplanetary Magnetic Field (IMF) turns southward ($B_z < 0$), allowing the electric field from the magnetosphere to penetrate the ionosphere. This process primarily influences the equatorial and low-latitude ionosphere, but also interacts with high-latitude regions, contributing to changes in the auroral electrojet currents. These currents are represented by an increase in the *AE* index, which reflects enhanced auroral activity during geomagnetic storms. This electric field penetration exacerbates electron distribution disturbances in the ionosphere, driving ionospheric irregularities (Tsurutani et al., 2008; Astafyeva et al., 2016). In the study by Srinivasu et al. (2019), it is mentioned that PPEF enhances the occurrence of scintillation, with observational results showing increased L-band scintillation in GPS and GLONASS signals during the main phase of the geomagnetic storm. Therefore, PPEF is crucial in understanding the impact of solar wind on Earth's ionosphere, especially during geomagnetic events, as it influences ionospheric irregularities and triggers stronger scintillation in radio signals.

The E_y is calculated based on IMF and solar wind velocity measurements captured by satellite at L1 Lagrangian point, and the electric field derived through the Lorentz transformation (Parks, 2003). Within the solar wind reference frame, the electric field is zero. The E_y arises due to the motion of solar wind plasma relative to the satellite. This transformation is represented by the equation

$$E_y = -(V_z B_x - V_x B_z),$$

where V represents the solar wind flow speed, while IMF is denoted by B. An orthogonal coordinate system defines the direction, with the *X*-axis pointing towards the Sun, the *Y*-axis pointing towards dusk, and the *Z*-axis following the right-hand rule. The pre-2021 solar wind component data is obtained from the ACE satellite, and from the NOAA satellite for data from 2021 onward.

2.2 S4 Index Data

Ionospheric scintillation refers to rapid variations in the intensity and phase of GNSS signals due to fluctuations in electron density in the ionosphere (Yeh and Liu CH, 1982). This parameter detects small instabilities that can disrupt satellite-based communication and navigation systems. Ionospheric scintillation is measured using the S4 index, which is obtained from the following equation (Dubey et al., 2006)

$$\text{S4 Index} = \sqrt{\text{S4}^2 - \text{S4corr}^2}.$$

The total S4 that can be measured is denoted as S4, while S4corr is the value of S4 that has been corrected for thermal noise. S4 is the normalized standard deviation of the received signal power intensity (Davies, 1990). Strong scintillation is indicated by an S4 index where S4 > 0.5, indicating a considerable disturbance of the ionospheric scintillation. On the other hand, weak scintillation is associated with an S4 index value of S4 < 0.25, while moderate scintillation values fall in the 0.25 < S4 < 0.5 range (Butcher, 2005; Carrano et al., 2019).

This study uses S4 data from GNSS receiver instruments at seven observation stations spread across Indonesia's eastern to western regions, as shown in Figure 1. The coordinates of each station are as follows: PTK (0.04°S, 109.34°E geographic; 9.41°S magnetic), KTB (0.202°S, 100.32°E geographic; 9.34°S magnetic), BDG (6.89°S, 107.59°E geographic; 16.06°S magnetic), SMD (6.90°S, 107.83°E geographic; 16.07°S magnetic), KPG (10.21°S, 123.66°E geographic; 18.97°S magnetic), MND (1.44°N, 124.84°E geographic; 7.35°S magnetic), and BIK (1.18°S, 136.10°E geographic; 9.23°S magnetic). The time difference between the farthest stations, from east to west, is 2 hours UTC. S4 data were collected from 2003 to 2024, although some data gaps were due to equipment malfunctions at specific periods or locations. This long observation period is expected to minimize the impact of the data gaps.

The S4 data received by the GNSS receiver antenna contains the influence of multipath effects. This occurs when the GNSS signal is reflected by surfaces such as the ground, buildings, or water prior

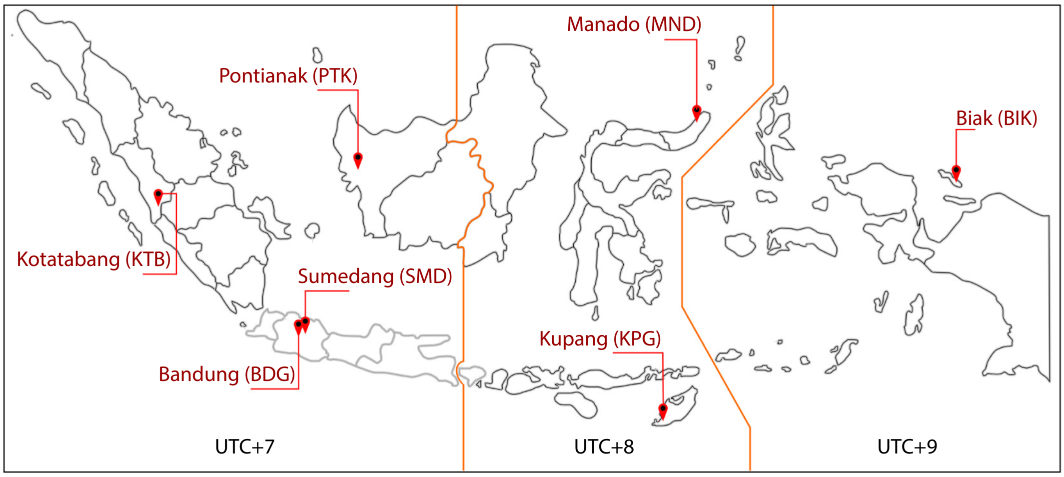

Figure 1. GNSS receiver stations in Indonesia.

to reaching the receiver antenna, resulting in additional signal paths. As a result, the received signal combines both the direct (line-of-sight) and the reflected signals. The multipath effect on the S4 data can resemble ionospheric fluctuations. The presence of multipath effects in the data makes distinguishing between ionospheric disturbances and reflection effects complex. Therefore, multipath reduction is performed to ensure that the data being analyzed accurately represents the ionospheric conditions, and to avoid misinterpretation in the data analysis. To reduce the multipath effect, a data filter is applied using S4 data with an elevation angle greater than 30 degrees (Carrano et al., 2019).

The data generated also contains noise, which reduces the accuracy of the analysis. The noise is identified by observing anomalies in the daily variation graphs of the S4 indices, after which each data point is cleaned manually. The noise in the S4 index data is shown in Figure 2 below, before the noise filtering process, which enhances the data quality in preparation for analysis.

2.3 Analysis Method

The analytical method used in this study is the Superposed Epoch Analysis (SEA), first introduced by Chree (1913). This technique can be utilized to analyze and evaluate recurring patterns observed in natural phenomena, such as geomagnetic storms and meteorological events. The first step in using this method is determining the epoch 0 point, which serves as the reference time point. Subsequently, data is collected from periods before and after the predetermined epoch 0 point. Each event is aligned with the same epoch 0 point to identify recurring patterns. The purpose of aligning data to this common reference point is to identify general patterns that may not be apparent when analyzing individual events.

The application of the SEA method in this study is as follows. The epoch 0 point is determined based on the minimum SYM-*H* index value for each geomagnetic storm event, a method previously applied by Sori et al. (2021). The selection of minimum SYM-*H* as epoch 0 represents the peak phase of the geomagnetic storm, corresponding to the strongest ring current and the most significant disturbance in the Earth's magnetosphere. Previous studies used dSYM-*H*/*dt* to determine the onset of storm-time electric field penetration (Ram et al., 2008; Jain et al., 2010), effectively identifying short-term geomagnetic variations. In contrast, this study uses minimum SYM-*H* as epoch 0 because it is more suitable for analyzing the entire main and recovery phases of geomagnetic storms. This approach provides a broader assessment of ionospheric disturbances rather than focusing solely on the initial effects of electric field penetration. The 1-minute resolution of SYM-*H* is consistent with the temporal resolution of the S4 index, ensuring a precise comparison between geomagnetic activity and ionospheric irregularities. Maintaining consistency in temporal resolution strengthens the reliability of the analysis and provides a clearer understanding of ionospheric responses to intense geomagnetic storm events.

The data were analyzed over 72 hours before and after the epoch 0 point. For example, during the geomagnetic storm event on April 24, 2012, the minimum SYM-*H* index value was recorded at −125 nT at 03:30:00 UTC. This time, corresponding to the minimum

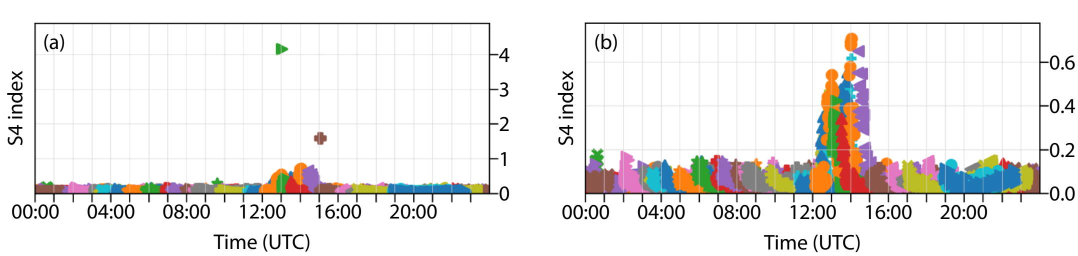

Figure 2. Example of plotting the S4 index at the Pontianak station, on April 12, 2012: (a) Data before noise filtering; (b) S4 data after noise filtering.

SYM-*H* value, was used to determine the epoch 0 point for the geomagnetic storm event, with data collected from April 21, 2012, at 03:30:00 UTC, to April 27, 2012, at 03:29:00 UTC. The determination of the epoch 0 point and the 72-hour range before and after was conducted under the condition that the expansion and recovery phases of the geomagnetic storm did not overlap with other geomagnetic storm events. This was to ensure that the ionospheric response analyzed in this study originated solely from a single geomagnetic storm, and was not influenced by magnetic field fluctuations from two consecutive geomagnetic storms.

The next step involves superposing the epoch 0 point of each geomagnetic storm event using the SEA method to clarify the pattern. As a continuation of Figure 3, an example of using the SEA method for the SYM-*H* parameter from several geomagnetic storm events in April 2012 can be seen in Figure 4, where the *X*-axis represents time in UTC.

Finally, geomagnetic data, solar wind components, and the S4 index were superposed based on the epoch 0 times for each geomagnetic storm event. The average of each parameter was calculated to illustrate variation patterns during geomagnetic storms, covering both the storm's expansion and recovery phases.

3. Results and Discussion

During the period from 2003 to 2024, a total of 419 geomagnetic storm events were identified based on the *Dst* index. These events were analyzed to investigate the ionospheric response to geomagnetic storms, which were categorized into two groups based on their geomagnetic storm strength. Geomagnetic storms with a minimum *Dst* index value of −100 nT ≤ min. *Dst* ≤ −30 nT were classified as weak-moderate geomagnetic storms, while storms with a minimum *Dst* index value ≤ −100 nT were classified as strong geomagnetic storms. According to the geomagnetic storm classification by Loewe and Prolss (1997), the weak-moderate category includes weak and moderate storms, whereas the strong category encompasses strong, severe, and great storms. The great geomagnetic storm in May 2024 was included in the analysis as one of the most intense in recent decades. These categories were determined to provide a basis for analyzing the ionospheric response to geomagnetic storms of varying strengths. In this study, the *Dst* index was used only for classifying geomagnetic storms, and not for evaluating their overall characteristics.

Previous studies have shown that the ionospheric scintillation response depends on the local time of the geomagnetic storm peak (Spogli et al., 2016; Marlia et al., 2019; Putra et al., 2023). To further investigate this dependence, we initially considered data from seven observation stations across three different time zones (UTC+7, UTC+8, and UTC+9). However, to ensure consistency in local time interpretation and minimize variations due to time zones, we focused our analysis on four stations in the UTC+7 time zone: KTB, PTK, BDG, and SMD. This selection allows us to assess better the potential dependence of scintillation response on the local time of minimum SYM-*H* while reducing biases from time zone differences. These four stations were also selected because they have higher data availability and cover more events than the other three stations. To systematically examine this dependence, the time of minimum SYM-*H* was grouped into eight 3-hour intervals, covering the full 24-hour period. For reference, these intervals correspond to local time (UTC+7) at the observation stations, such as 00:00–03:00 UTC (07:00–10:00 LT), 03:00–06:00 UTC (10:00–13:00 LT), and so on.

3.1 Weak-Moderate Geomagnetic Storm Events

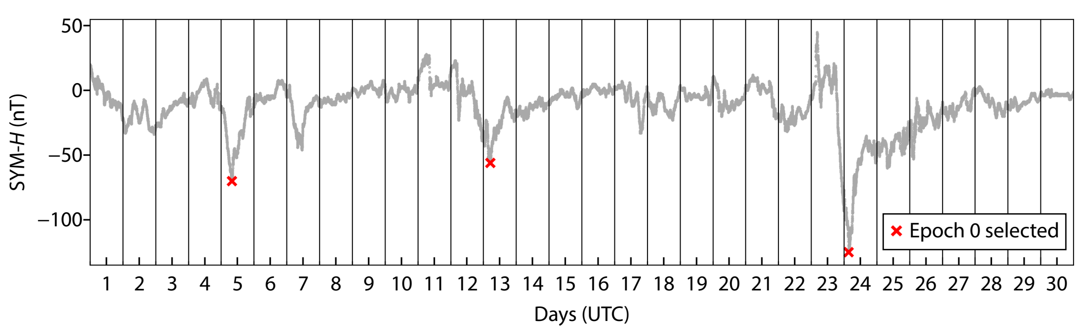

Figure 3. Example of determining the epoch 0 point, based on the SYM-*H* parameter for April 2012.

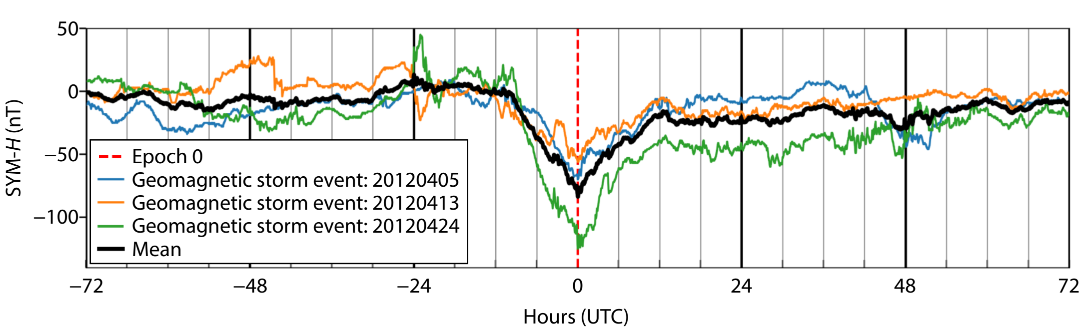

Figure 4. An example of using the SEA method for the SYM-*H* parameter was in April 2012.

A total of 357 geomagnetic storm events in the weak-moderate category were recorded during the study period. Geomagnetic, solar wind, and ionospheric scintillation parameters during the geomagnetic storm events are displayed in Figure 5 using the SEA method. The black lines in Figures 5a through 5e represent the average of each parameter, providing a depiction of similar patterns. The dashed red vertical line in the center of the figure marks the epoch 0 point (minimum SYM-*H*).

The rapid variations in intensity and phase of the signal, indicated by fluctuations in electron density, are interpreted through the variation patterns of the S4 index visualized in Figure 5f. An S4 index value above 0.5 indicates strong ionospheric scintillation.

The patterns of each parameter in Figures 5a through 5e are represented as averages that peak as they approach the epoch 0 point. The SYM-*H* index shows an average of about −15 nT up to 8 hours before epoch 0. Over time, its value decreases, reaching an average minimum of about −64 nT exactly at epoch 0, and then gradually increases, reaching around −15 nT by the second day.

The average B_z and E_y values peak about −7 nT and ~0.9 mV/m, respectively, about 2 hours before epoch 0. Both parameters are almost constant, with only slight fluctuations about 6 hours after epoch 0. The *AE* index shows a different peak time, around 1 hour before epoch 0, with an average of ~750 nT, afterwards followed by a small fluctuation of about 18 to 24 hours.

The average S4 index from all stations for the weak-moderate geomagnetic storm category is shown in Figure 5f. Scintillation is not observed in the first 6 hours after epoch 0, but strong scintillation appears near epoch 0. Afterward, strong scintillation first appears ~6 hours after epoch 0. At the onset of scintillation (~6 hours after epoch 0), the E_y parameter shows an average of

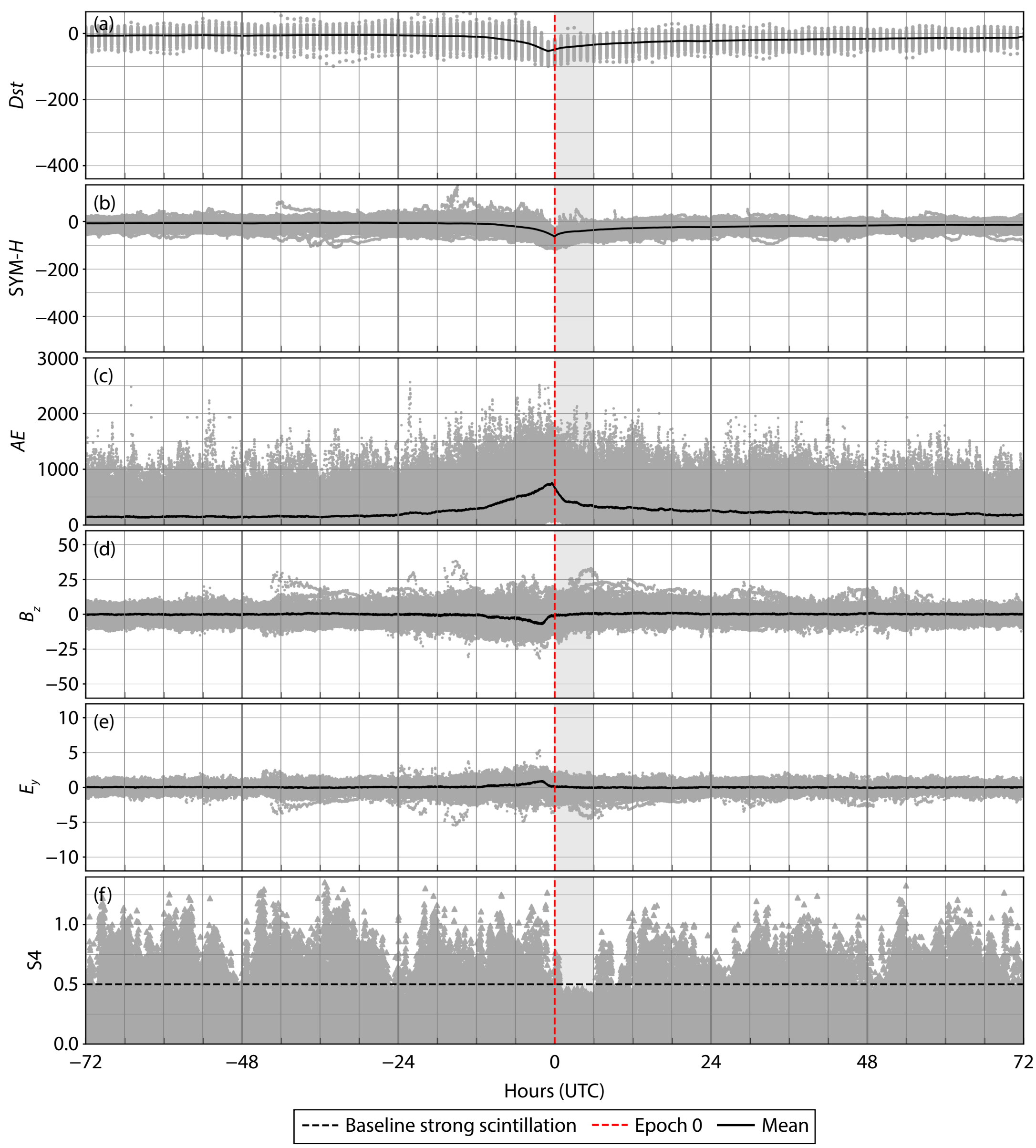

Figure 5. Geomagnetic condition, solar wind, and S4 index during weak-moderate geomagnetic storms (2003–2024). Panel figures describe: (a) *Dst*, (b) SYM-*H*, (c) *AE*, (d) B_z, (e) E_y, and (f) S4 index, respectively.

about −0.036 mV/m. At the same time, the SYM-*H* and *AE* indices display averages of about −36 nT and 330 nT, respectively. Based on this observation, we suspect that E_y is not a significant determinant of scintillation events due to its relatively small magnitude. As shown in Figure 5e, the average fluctuation of the interplanetary electric field is minimal.

Figure 6 presents subplots of Figure 5f, categorized by the local time (UTC+7) of minimum SYM-*H* during weak-moderate geomagnetic storms. Key markers at 19:00 LT (Green) and 06:00 LT (Magenta) indicate specific local times associated with observed scintillation variations. The 19:00 LT (post-sunset) marker suggests a period when increased scintillation is frequently observed. Meanwhile, the 06:00 LT (pre-sunrise) marker represents a time when scintillation can also be observed, although less often because the ionosphere becomes exposed to sunlight, which increases electron density and reduces the fluctuations that cause scintillation.

Figures 6a–6c illustrate the occurrence patterns of ionospheric scintillation when the storm peak occurred between morning and afternoon (07:00–16:00 LT), during daytime hours. In Figure 6a, where the minimum SYM-*H* occurred between 07:00–10:00 LT, strong scintillation was first observed ~10 hours after epoch 0. In Figure 6b (10:00–13:00 LT), scintillation appeared slightly earlier, at ~9 hours after epoch 0. Meanwhile, in Figure 6c (13:00–16:00 LT), the S4 index increased as early as ~6 hours after epoch 0. These figures demonstrate that ionospheric scintillation continues to develop from dusk into nighttime local hours, even during the recovery phase of geomagnetic storms.

Figures 6d and 6e represent cases where the minimum SYM-*H* occurred between before local sunset and nighttime (16:00–22:00 LT). In Figure 6d (16:00–19:00 LT), scintillation appeared

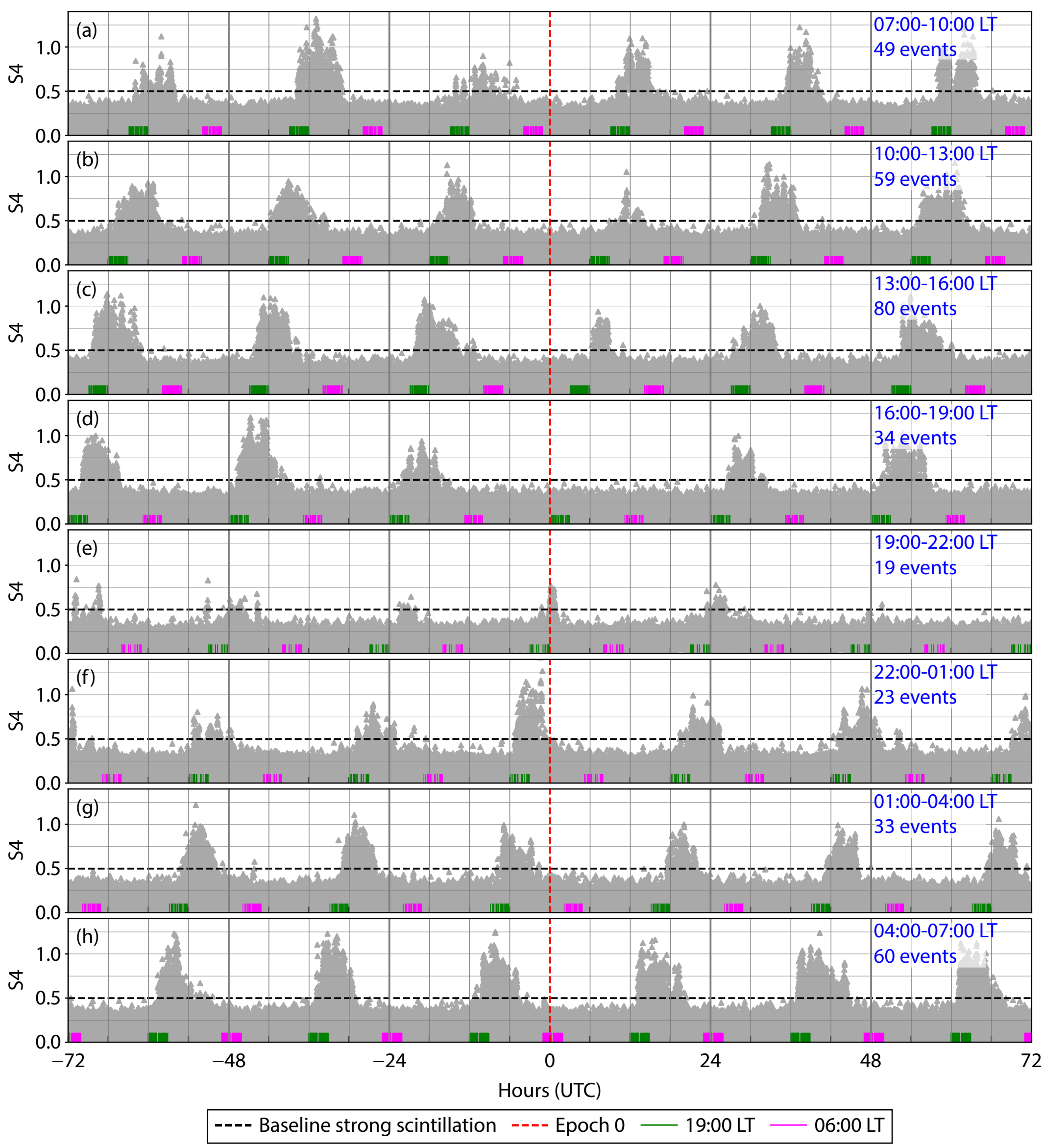

Figure 6. Occurrence of ionospheric scintillation based on local time (UTC+7) of minimum SYM-*H* for weak-moderate geomagnetic storms (2003–2024). Panel figures describe: (a) 07:00–10:00 LT, (b) 10:00–13:00 LT, (c) 13:00–16:00 LT, (d) 16:00–19:00 LT, (e) 19:00–22:00 LT, (f) 22:00–01:00 LT, (g) 01:00–04:00 LT, (h) 04:00–07:00 LT.

much later, ~26 hours after epoch 0, and no significant increase in the S4 index was observed during either the main or recovery phase of the storm. This suggests a delayed ionospheric scintillation response when the storm minimum occurs near sunset. In contrast, Figure 6e (19:00–22:00 LT) shows that scintillation began developing a few hours before epoch 0, weakened as the storm entered the recovery phase, and was no longer observed from post-midnight to sunrise. However, scintillation reappeared the following evening, ~23 hours after epoch 0. This indicates that scintillation development can be delayed until the next night, even as the storm progresses into its recovery phase.

Figures 6f through 6h illustrate cases where the minimum SYM-*H* occurred between nighttime and sunrise (22:00–07:00 LT). In Figure 6f (22:00–01:00 LT), strong scintillation was first observed ~19 hours after epoch 0. At later hours, when the minimum SYM-*H* occurred closer to midnight to sunrise, scintillation was detected earlier. In Figure 6g (01:00–04:00 LT), scintillation began increasing ~17 hours after epoch 0, whereas in Figure 6h (04:00–07:00 LT), it appeared as early as ~13 hours after epoch 0. Scintillation was also observed a few hours before the storm peak, particularly during the main phase when sunset coincided with storm activity, before gradually weakening as it approached epoch 0. However, scintillation was no longer observed from post-midnight to pre-sunrise. These figures indicate that ionospheric scintillation can develop even before the storm reaches its peak phase. This suggests that scintillation can persist from sunset into nighttime, even as the storm progresses through its main phase. Although the onset time varies, the results consistently show that scintillation occurs the following evening.

These results indicate a clear dependence of ionospheric scintillation onset on the local time of minimum SYM-*H*, with distinct patterns observed at different time windows:

• For storms peaking between morning and afternoon (07:00–16:00 LT), ionospheric scintillation typically develops within ~6 to 10 hours after the storm peak, consistently occurring around post-sunset on the same day, even during the recovery phase of the storm.

• For storms peaking between late afternoon and early night (16:00–19:00 LT), scintillation is not observed on the same evening. Instead, it only appears ~26 hours after epoch 0, during the next day's sunset, suggesting a delayed scintillation response when the storm peak occurs near sunset.

• For storms peaking between nighttime and sunrise (19:00–07:00 LT), scintillation can still be observed a few hours before the storm peak, particularly during the main phase when sunset coincides with storm activity. However, scintillation gradually weakens as it approaches epoch 0 and is not observed from post-midnight to pre-sunrise, before reappearing during the following evening.

3.2 Strong Geomagnetic Storm Events

We analyzed 62 strong geomagnetic storm events. Figure 7 illustrates the same parameters as Figure 5, but for strong geomagnetic storms. Black lines are also presented in Figures 7a through 7e, representing the average for each parameter.

During this event, the fluctuations of SYM-*H*, *AE*, B_z, and E_y appear to be higher and faster as they approach epoch 0, compared to weak-moderate geomagnetic storms. This could indicate that the fluctuations of these four geomagnetic parameters are directly related to the strength of the geomagnetic storm. As shown in Figure 7b, SYM-*H* is about −15 nT, 9 hours before epoch 0. As SYM-*H* approaches epoch 0, it decreases to a minimum of −170 nT, then slowly increases to about −15 nT on the third day after epoch 0. SYM-*H* takes longer to return to its original condition during the recovery phase of the geomagnetic storm.

The B_z and E_y parameters show fluctuations lasting for several hours during the main phase of the geomagnetic storm, with the intensity of fluctuations increasing until they peak about 2 hours before epoch 0. The B_z and E_y peaks are about −17 nT and ~2.7 mV/m, respectively. Both parameters then decrease and become more stable, with only minor fluctuations occurring about 18 hours after epoch 0. The *AE* index also shows fluctuations during the main phase of the geomagnetic storm, increasing in magnitude as it approaches epoch 0. The peak of the *AE* index is observed about 1 hour before epoch 0, with a magnitude of ~1103 nT. More minor fluctuations are observed for at least 24 hours after epoch 0.

Figure 7f shows the average S4 index from all stations during strong geomagnetic storms. Based on the S4 index, ionospheric scintillation appears similar to that of weak-moderate geomagnetic storms, where no significant increase in the S4 index is detected around epoch 0. However, in the case of strong geomagnetic storms, ionospheric scintillation increases ~12 hours after epoch 0.

At the onset of scintillation (~12 hours after epoch 0), the averages of SYM-*H* and *AE* are about −75 nT and 360 nT, respectively. At the same time, the daytime E_y is ~0.35 mV/m, which is a relatively small value. This may indicate that the contribution of the dayside E_y to ionospheric scintillation is insignificant. Additionally, it may indicate that the auroral electrojet influences the delay in scintillation, which increases after the peak of the geomagnetic storm.

Figure 8 presents subplots of Figure 7f, and follows a similar interpretation as Figure 6, but instead focuses on strong geomagnetic storms. Key markers at 19:00 LT (Green) and 06:00 LT (Magenta) indicate specific local times associated with observed scintillation variations. The 19:00 LT (post-sunset) marker suggests a period when an increase in scintillation is frequently observed. Meanwhile, the 06:00 LT (pre-sunrise) marker represents a time when scintillation can also be observed, although less often, because the ionosphere becomes exposed to sunlight, which increases electron density and reduces the fluctuations that cause scintillation.

Figures 8a through 8c illustrate the occurrence patterns of ionospheric scintillation during strong geomagnetic storms, where the storm peak occurred between morning and local pre-sunset period (07:00–16:00 LT). In Figure 8a, where the minimum SYM-*H* occurred between 07:00–10:00 LT, the S4 index showed the earliest increase at ~12 hours after epoch 0. Strong scintillation can develop from dusk into nighttime on the same day during the recovery phase of the geomagnetic storm. Meanwhile, in Figure

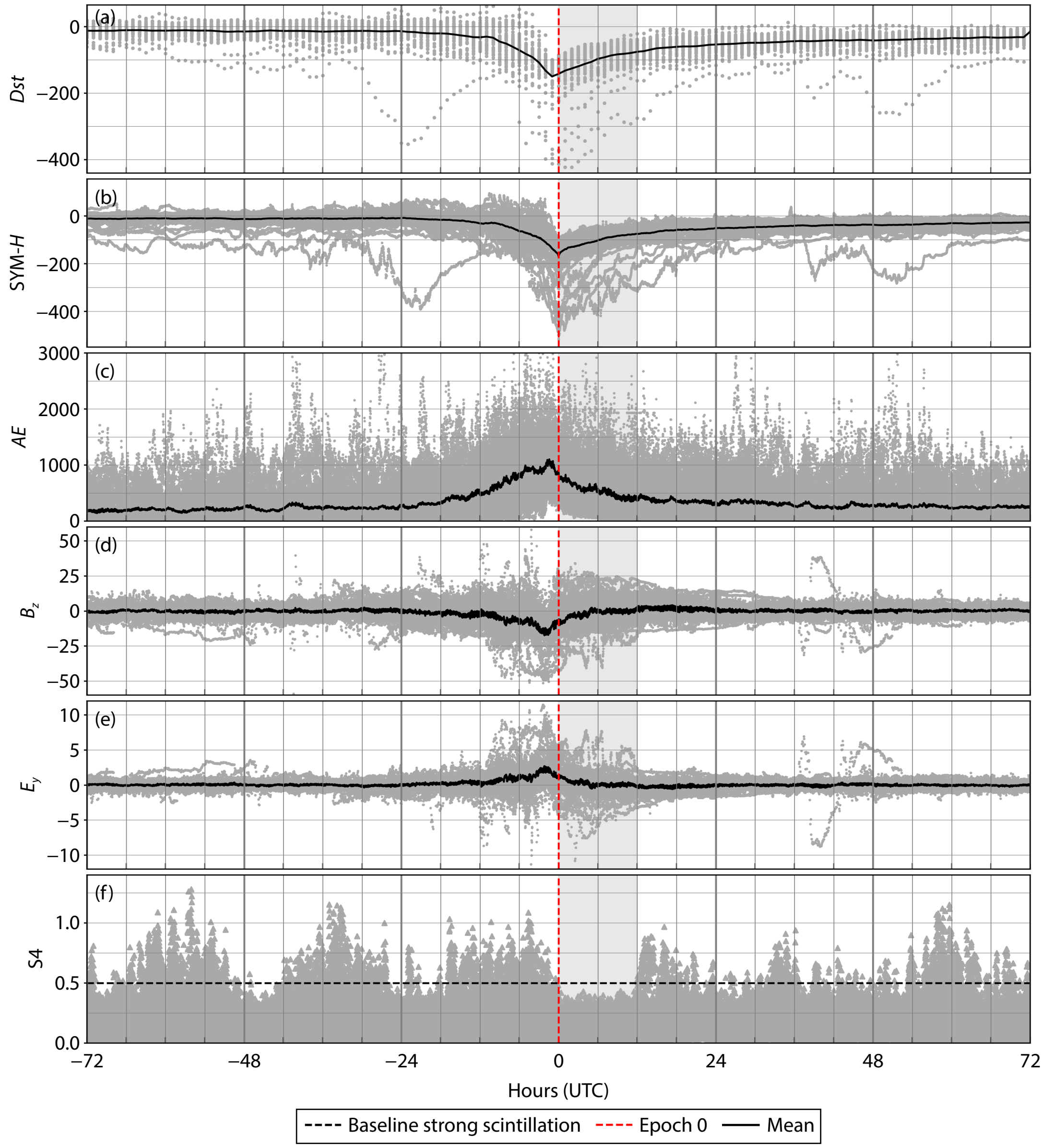

Figure 7. Geomagnetic condition, solar wind, and S4 index during strong geomagnetic storms (2003–2024). Panel figures describe: (a) *Dst*, (b) SYM-*H*, (c) *AE*, (d) B_z, (e) E_y, and (f) S4 index, respectively.

8b (10:00–13:00 LT), ionospheric scintillation was observed much later, ~31 hours after epoch 0. In Figure 8c (13:00–16:00 LT), the S4 index showed a noticeable increase ~53 hours after epoch 0, indicating a significantly delayed response. The apparent difference in scintillation onset between Figures 8b and 8c, despite both having similar epoch 0 timings, suggests that the strength of geomagnetic storms plays a crucial role in modulating the response time of ionospheric scintillation.

Figures 8d and 8e represent cases where the minimum SYM-*H* occurred between the local pre-sunset period and nighttime (16:00–22:00 LT). In Figure 8d (16:00–19:00 LT), when ionospheric scintillation is more likely to develop due to post-sunset plasma bubble formation driven by the RTI, scintillation was first observed ~28 hours after epoch 0. However, unlike the earlier cases, no significant increase in the S4 index was observed during either the main or recovery phase of the storm, suggesting a delayed ionospheric scintillation response when the storm minimum occurs near sunset. In contrast, Figure 8e (19:00–22:00 LT) indicates that ionospheric scintillation developed a few hours before epoch 0, weakened as the storm transitioned from its peak to the recovery phase, and did not reappear from post-midnight to sunrise. However, scintillation was observed again ~25 hours after epoch 0, in the following evening.

Figures 8f–8h illustrate cases where the minimum SYM-*H* occurred between nighttime and sunrise (19:00–07:00 LT). In Figure 8f (22:00–01:00 LT), ionospheric scintillation was observed ~20 hours after epoch 0. At later hours, when the minimum SYM-*H* occurred closer to midnight to sunrise, scintillation was detected earlier. In Figure 8g (01:00–04:00 LT), scintillation began increasing ~17 hours after epoch 0, whereas in Figure 8h (04:00–07:00 LT), it appeared as early as ~15 hours after epoch 0. Scintillation was also observed a few hours before the storm peak, particularly

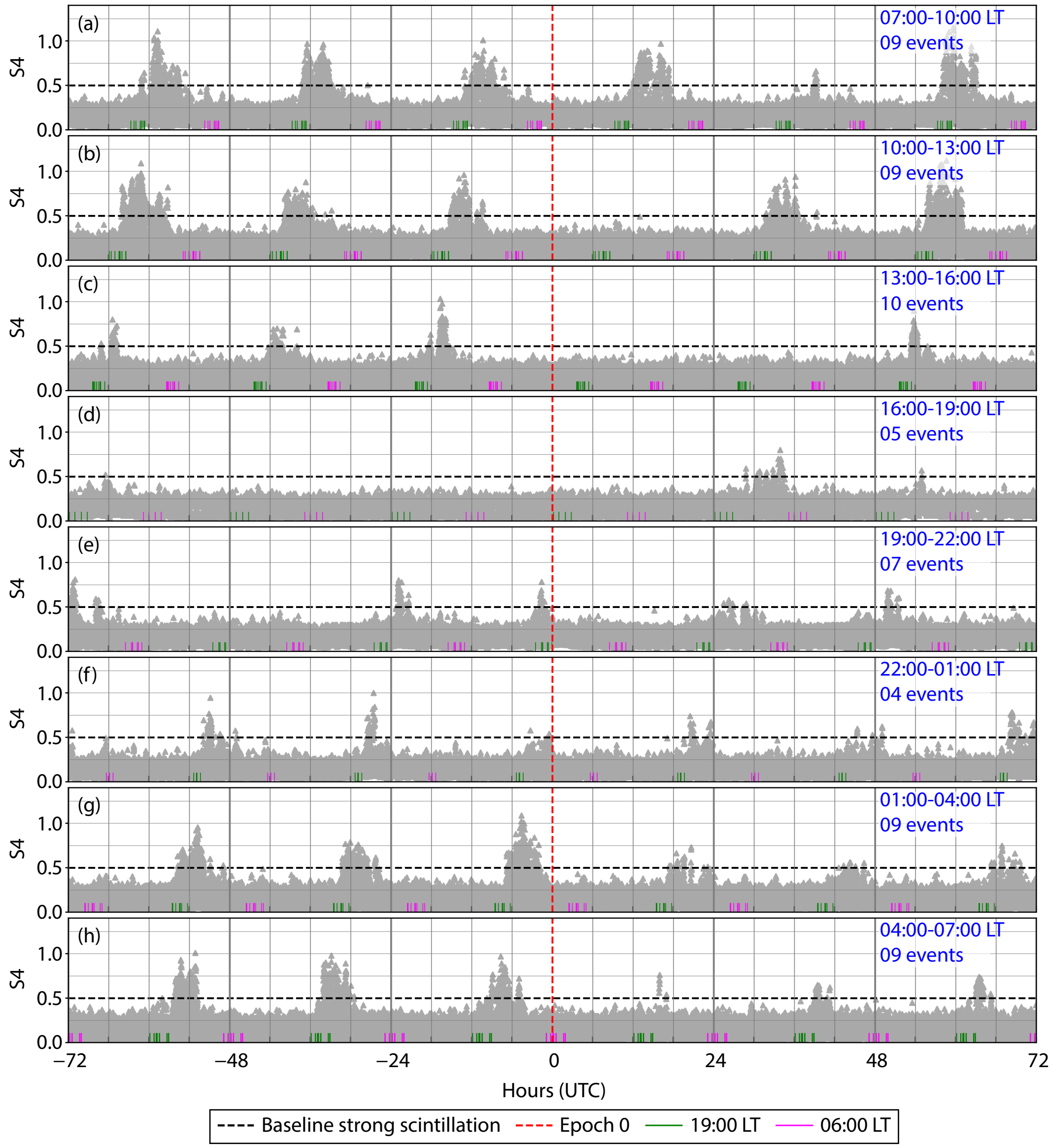

Figure 8. Occurrence of ionospheric scintillation based on the local time (UTC+7) of minimum SYM-*H* for strong geomagnetic storms (2003–2024). Panel figures describe: (a) 07:00–10:00 LT, (b) 10:00–13:00 LT, (c) 13:00–16:00 LT, (d) 16:00–19:00 LT, (e) 19:00–22:00 LT, (f) 22:00–01:00 LT, (g) 01:00–04:00 LT, (h) 04:00–07:00 LT.

during the main phase when sunset coincided with storm activity, before gradually weakening as it approached epoch 0. However, scintillation was no longer observed from post-midnight to pre-sunrise. These figures indicate that ionospheric scintillation can develop even before the storm reaches its peak phase. This suggests that scintillation can persist from sunset into nighttime, even as the storm progresses through its main phase. Although the onset time varies, the results consistently show that scintillation occurs the following evening.

These results indicate a clear dependence of ionospheric scintillation onset on the local time of minimum SYM-*H* during strong geomagnetic storms, with notable variations observed across different time windows.

• For storms peaking between morning and pre-sunset (07:00–16:00 LT; Figures 8a–8c), ionospheric scintillation typically develops between ~12 to 53 hours after epoch 0, with the onset time strongly dependent on storm intensity. When the minimum SYM-*H* occurs between 07:00–10:00 LT (Figure 8a), scintillation appears earlier (~12 hours after epoch 0), indicating that post-sunset EPBs can still form despite strong geomagnetic activity. However, when the storm peak occurs later in this window (10:00–16:00 LT; Figures 8b–8c), scintillation is significantly delayed, appearing up to ~53 hours after epoch 0, suggesting prolonged suppression of post-sunset EPBs.

• For storms peaking between pre-sunset and post-sunset (16:00–19:00 LT; Figures 8d), the most extended delay (~28 hours) is observed when the minimum SYM-*H* occurs between 16:00–19:00 LT (Figure 8d), reinforcing that geomagnetic storms during this window can strongly suppress ionospheric scintillation.

• For storms peaking between nighttime and sunrise (19:00–07:00 LT; Figures 8e–8h), ionospheric scintillation exhibits an earlier onset compared to other time windows, typically developing ~15 to 25 hours after epoch 0, depending on proximity to midnight. Scintillation occurrence before epoch 0 suggests that ionospheric irregularities can develop in the dusk-to-midnight sector before the storm reaches its peak, aligning with the 19:00 LT marker (Green), which signifies the role of PPEF in enhancing EPB formation. However, in contrast to previous interpretations, post-midnight scintillation is not observed after epoch 0 in this window. Instead, scintillation disappears from post-midnight to pre-sunrise, reappearing only in the following evening, reinforcing the idea that DDEF effects may not be sufficient to sustain ionospheric irregularities into the recovery phase of strong storms.

3.3 The Influence of Geomagnetic Storm Strength on the Ionospheric Scintillation Response in Indonesia

To understand the occurrence patterns of ionospheric scintillation during geomagnetic storms in Indonesia, we applied the SEA method to multiple storm events from 2003 to 2024 using data from seven GNSS stations. The results indicate that the delay in scintillation onset strongly depends on both storm strength and the local time of the minimum SYM-*H*, which is defined as epoch 0 in our SEA method. During strong geomagnetic storms, scintillation is significantly delayed, with the earliest occurrence observed ~12 hours after epoch 0 (Figure 7). In contrast, for weak-moderate geomagnetic storms, scintillation occurs much earlier, with the earliest occurrence observed ~6 hours after epoch 0 (Figure 5). However, this pattern does not hold consistently across all events. Instead, the local time of the minimum SYM-*H* plays a crucial role in determining whether scintillation is significantly suppressed or can develop earlier. Specifically, when epoch 0 occurs during specific local time windows, scintillation is either delayed or completely absent, indicating that background ionospheric conditions and storm-driven electric fields jointly influence post-storm scintillation behavior.

Furthermore, the delay in ionospheric scintillation onset is not only dependent on storm strength but also on the local time at which the minimum SYM-*H* occurs. The analysis in Figures 6 and 8 provides detailed insights into ionospheric scintillation occurrence during geomagnetic storms from 2003 to 2024, based on the local time (UTC+7) of the minimum SYM-*H*. For weak-moderate geomagnetic storms, scintillation appears earliest (~6 hours after epoch 0) when the minimum SYM-*H* occurs between 13:00–16:00 LT. Meanwhile, for strong geomagnetic storms with a minimum SYM-*H* occurring between 07:00–10:00 LT, scintillation enhancement is observed earliest (~12 hours after epoch 0). The ionospheric scintillation response to a minimum SYM-*H* occurring at 07:00–10:00 LT for both storm categories (Figures 6a and 8a) suggests that storms peaking during this period do not significantly suppress scintillation. This indicates that EPBs can still develop as the ionosphere transitions into nighttime conditions.

The most pronounced delay in scintillation onset is observed during strong geomagnetic storms when the minimum SYM-*H* occurs between daytime and pre-sunset hours (10:00–16:00 LT), as shown in Figures 8b and 8c. In these cases, scintillation does not appear until the following day's sunset, indicating an extended suppression of plasma bubble growth. Conversely, for weak-moderate geomagnetic storms occurring within the same local time window (Figures 6b and 6c), scintillation can still develop by sunset on the same day, suggesting a weaker suppression effect. Additionally, when the minimum SYM-*H* occurs between pre-sunset and post-sunset hours (16:00–19:00 LT), scintillation is almost entirely absent in both storm categories (Figures 6d and 8d), regardless of whether the storm is in its main or recovery phase. This absence suggests that ionospheric conditions during this period are particularly unfavorable for plasma bubble development, likely due to the dominance of westward-directed electric fields and suppressed vertical plasma drift. When the minimum SYM-*H* occurs between post-sunset and sunrise (19:00–07:00 LT), scintillation can still be observed a few hours before the storm peak, particularly during the main phase in both storm categories (Figures 6e–h, 8e–h). This indicates that scintillation can develop and persist even during the main phase of a geomagnetic storm, up until the storm reaches its peak.

This pattern is consistent with the findings of Sori et al. (2021), which demonstrated that the occurrence of plasma bubbles and variations in the Rate of TEC Index (ROTI) strongly depend on the storm phase and local time. During the main phase of a geomagnetic storm, the enhancement of PPEF strengthens PRE, accelerating Rayleigh–Taylor Instability (RTI) growth and facilitating the formation of plasma bubbles in the dusk-to-midnight sector after sunset (Ma GY and Maruyama, 2006; Cherniak and Zakharenkova, 2016; Aa et al., 2018; Li G et al., 2018). Many studies have shown that storm-time plasma bubbles tend to form in the dusk sector due to the intensification of eastward electric fields, which enhance vertical plasma drift and increase ROTI values, indicating stronger plasma density irregularities (Fejer et al., 1999; Sori et al., 2021). Additionally, the uplift of plasma bubbles to higher altitudes under these conditions may allow them to persist longer than usual, sometimes extending into post-midnight hours.

However, during the recovery phase, the dominant electrodynamic mechanisms change. The influence of over-shielding penetration electric fields and DDEF become more pronounced, replacing the role of PPEF in controlling ionospheric plasma dynamics. These westward-directed electric fields weaken PRE, reducing RTI growth rates and suppressing plasma bubble development in the dusk sector (De La Beaujardière et al., 2009; Abdu, 2012; Li J et al., 2012). The suppression of plasma bubbles in this sector is reflected in a gradual decline in ROTI values within 1 to ~13 hours after the minimum SYM-*H*, indicating a reduction in ionospheric density irregularities. In contrast, during the same recovery phase, ROTI values increase in the post-midnight sector within 1 to ~11 hours after minimum SYM-*H*. This suggests that while plasma bubble formation is inhibited in the dusk sector, it may persist or even intensify in the pre-dawn sector, where eastward-directed electric fields remain dominant (Fejer et al., 2008; Sori et al., 2021). Since plasma bubbles are closely linked to ionospheric scintillation through small-scale density irregularities, these variations in ROTI reflect corresponding changes in scintillation activity.

The suppression of scintillation in the dusk-to-midnight sector during the recovery phase is primarily due to the weakening of PRE, which reduces the RTI growth rate and inhibits EPB formation, as also suggested by Fejer et al. (2008). Since ionospheric scintillation is closely linked to small-scale electron density irregularities, its occurrence is modulated by the same electrodynamic mechanisms that regulate EPB growth and suppression. During strong geomagnetic storms, when minimum SYM-*H* occurs between 10:00–16:00 LT, scintillation is significantly delayed until the following day's sunset due to the dominance of DDEF and over-shielding penetration, which generate westward electric fields in the dusk sector, weakening PRE and suppressing plasma bubble formation. The weakened PRE leads to a reduced RTI growth rate, preventing EPBs from forming until ionospheric conditions recover the next day. In contrast, during weak-moderate geomagnetic storms, the suppression effect is weaker due to the less intense storm-induced electric fields. When minimum SYM-*H* occurs within the same local time window (10:00–16:00 LT), scintillation can still develop by sunset on the same day, suggesting that although DDEF and over-shielding effects are present, they are not strong enough to suppress PRE completely, allowing some degree of EPB growth. When minimum SYM-*H* occurs between 16:00–19:00 LT, scintillation is almost absent in both storm categories due to the peak influence of westward electric fields generated by DDEF and over-shielding, which drastically weaken PRE and inhibit EPB growth. Unlike the scintillation delay observed at 10:00–16:00 LT during weak-moderate storms, where scintillation can still develop on the same day, this condition is entirely unfavorable for plasma bubble formation until the storm enters the recovery phase, resulting in a complete absence of scintillation even as the storm subsides.

Conversely, when minimum SYM-*H* occurs between 19:00–07:00 LT, the likelihood of post-sunset EPB and scintillation increases due to the enhancement of PPEF, which strengthens PRE and reinforces RTI growth, allowing plasma bubbles to develop more efficiently in the dusk-to-midnight sector, leading to sustained scintillation activity even before the storm reaches its peak. These findings align with those of Sori et al. (2021), who demonstrated that storm-time PPEF enhances PRE and promotes plasma bubble formation in the dusk sector during the main phase. In contrast, DDEF and over-shielding effects suppress plasma bubbles in the dusk sector during the recovery phase. The suppression of EPBs in the dusk sector due to westward electric fields during the recovery phase contributes to the observed delay in the onset of S4 enhancement. Additionally, our results suggest that *AE* activity is crucial in controlling the delay in scintillation onset, particularly in the post-minimum SYM-*H* period.

As shown in Figures 5 and 7, the delay in scintillation onset is more pronounced when *AE* activity remains high after the minimum SYM-*H*. Our results indicate that scintillation first appears ~6 hours after epoch 0 in weak-moderate geomagnetic storms, and ~12 hours after epoch 0 in strong geomagnetic storms. The average *AE* index returns to its baseline value (quiet condition) ~6 and ~12 hours after epoch 0 for weak-moderate and strong geomagnetic storms, respectively, marking the general transition toward ionospheric recovery. This suggests that auroral activity contributes to the persistence of westward-directed electric fields in the equatorial region.

High *AE* activity is generally associated with stronger disturbance dynamo electric field (DDEF), which can prolong the suppression of PRE and delay the onset of post-storm ionospheric irregularities. When the local sunset coincides with epoch 0, post-sunset EPBs and scintillation are more likely to be suppressed due to the prolonged operation of DDEF-driven westward electric fields, inhibiting vertical plasma drift. Conversely, when *AE* activity is lower after the minimum SYM-*H*, the disturbance dynamo weakens more rapidly, allowing the PRE electric field to recover sooner, facilitating earlier plasma bubble growth and scintillation onset. This scenario is more likely to occur when epoch 0 falls within midnight to early morning, allowing scintillation to develop before epoch 0. However, post-midnight scintillation is not observed in the equatorial region during the recovery phase, for neither weak-moderate nor strong storm events.

These findings highlight the importance of considering both auroral activity and storm phase timing in assessing scintillation occurrence, particularly in the equatorial ionospheric prediction model. These findings also reinforce the importance of considering storm strength and local time variations when assessing ionospheric responses to geomagnetic disturbances. The results of the present study support the idea that daytime geomagnetic disturbances intensify westward electric fields, which persist into the evening sector and inhibit plasma bubble formation. In contrast, when the minimum SYM-*H* occurs during nighttime to early morning hours, scintillation can still develop before the storm peak, suggesting that pre-existing ionospheric conditions may contribute to earlier scintillation occurrence. These results provide critical insights into the role of storm phase and local time in modulating equatorial scintillation, offering valuable information for improving ionospheric scintillation prediction models with space weather applications.

4. Conclusions

This study analyzed the occurrence patterns of ionospheric scintillation during geomagnetic storms in Indonesia from 2003 to 2024, using SEA applied to GNSS data from seven stations. The results highlight that scintillation delay depends not only on storm strength, but also on the local time of the minimum SYM-*H*, demonstrating that background ionospheric conditions significantly influence storm-time plasma dynamics.

For weak-moderate storms, scintillation typically emerges ~6 hours after the minimum SYM-*H* when it occurs at 13:00–16:00 LT, while for strong storms, scintillation appears ~12 hours after the minimum SYM-*H* when it occurs at 07:00–10:00 LT. Scintillation is almost absent when the minimum SYM-*H* coincides with local sunset (16:00–19:00 LT), likely due to DDEF-induced suppression of EPB growth, which persists for at least 6 hours (weak-moderate storms) and 12 hours (strong storms) post-minimum SYM-*H*. Conversely, when the minimum SYM-*H* occurs at nighttime or early morning (19:00–07:00 LT), scintillation is observed before the storm peaks, suggesting that PPEF-driven plasma bubble formation plays a key role in this period.

Additionally, our findings emphasize the role of auroral activity (*AE* index) in modulating scintillation suppression duration. When *AE* activity remains high post-minimum SYM-*H*, DDEF persists longer, further delaying EPB formation and ionospheric recovery. The *AE* index returns to baseline ~6 hours (weak-moderate storms) and ~12 hours (strong storms) post-minimum SYM-*H*, marking the transition to post-storm conditions. These results underscore the global coupling between high-latitude auroral dynamics and low-latitude ionospheric irregularities.

Future studies should investigate the impact of seasonal variations, solar cycle influences, and multi-instrument observations (e.g., space-based and ionospheric radar measurements) to refine storm-time scintillation models further. These advancements will enhance space weather forecasting and GNSS-based applications, which are crucial for mitigating signal degradation in equatorial regions.

Acknowledgements

This research was supported by the National Research and Innovation Agency (BRIN), Indonesia. The authors thank the Pontianak Observation Station, and the National Research and Innovation Agency (BRIN), for their data support and dedication to maintaining the instruments in Pontianak. Special thanks are also extended to the Geophysics Laboratory, Department of Physics, Faculty of Mathematics and Natural Sciences, Universitas Gadjah Mada (UGM) for providing facilities, technical assistance, and valuable suggestions throughout the research process. One of the authors, Prayitno Abadi, expresses gratitude for Telkom University's support through the Research Collaboration Memorandum of Understanding on Regional Ionospheric Observation (No: 092/SAM3/TE-DEK/2021).

The main research data were generously provided by BRIN and the Institute for Space-Earth Environmental Research, Nagoya University. Geomagnetic data were obtained from the World Data Center (WDC) for Geomagnetism, Kyoto. Solar wind parameters were sourced from the Advanced Composition Explorer (ACE) satellite for data before 2021 and the National Oceanic and Atmospheric Administration (NOAA) for data from 2021 onwards. We sincerely thank all institutions for their invaluable contributions to the success of this study.

References

Aa, E., Huang, W. G., Liu, S., Ridley, A., Zou, S. S., Shi, L. Q., Chen, Y. H., Shen, H., Yuan, T. J., … Wang, T. (2018). Midlatitude plasma bubbles over China and adjacent areas during a magnetic storm on 8 September 2017. *Space Weather, 16*(3), 321–331. https://doi.org/10.1002/2017sw001776

Abadi, P., Saito, S., and Srigutomo, W. (2014). Low-latitude scintillation occurrences around the equatorial anomaly crest over Indonesia. *Ann. Geophys.*, *32*(1), 7–17. https://doi.org/10.5194/angeo-32-7-2014

Abadi, P., Otsuka, Y., Saito, S., Yamamoto, M., Perwitasari, S., Muafiry, I. N., Putra, A. Y., and Faturahman, A. (2024). Longitudinal range of the eastward-traveling equatorial plasma bubble inducing ionospheric scintillation. *Space Weather*, *22*(8), e2024SW003908. https://doi.org/10.1029/2024SW003908

Abadi, P., Muafiry, I. N., Pratama, T. N., Putra, A. Y., Suraina, Pramono, G. H., Wibowo, S. T., Chabibi, F. F., Ahmad, U. A., … Asnawi. (2025). Leveraging ROTI map derived from Indonesian GNSS receiver network for advancing study of Equatorial Plasma Bubble in Southeast/East Asia. *Earth Planet. Phys.*, *9*(1), 101–116. https://doi.org/10.26464/epp2025007

Abdu, M. A. (2012). Equatorial spread F/plasma bubble irregularities under storm time disturbance electric fields. *J. Atmos. Solar-Terrestr. Phys., 75–76*, 44–56. https://doi.org/10.1016/j.jastp.2011.04.024

Astafyeva, E., Zakharenkova, I., and Alken, P. (2016). Prompt penetration electric fields and the extreme topside ionospheric response to the June 22–23, 2015 geomagnetic storm as seen by the Swarm constellation. *Earth Planets Space*, *68*(1), 152. https://doi.org/10.1186/s40623-016-0526-x

Basavaiah, N. (2011). *Geomagnetism: Solid Earth and Upper Atmosphere Perspectives* (pp. 167). Dordrecht: Springer.

Bergin, A., Chapman, S. C., and Gjerloev, J. W. (2020). *AE, D_{ST}*, and their SuperMAG counterparts: the effect of improved spatial resolution in geomagnetic indices. *J. Geophys. Res.: Space Phys.*, *125*(5), e2020JA027828. https://doi.org/10.1029/2020JA027828

Burton, R. K., McPherron, R. L., and Russel, C. T. (1975). An empirical relationship between interplanetary conditions and *Dst*. *J. Geophys. Res.*, *80*(31), 4204–4214. https://doi.org/10.1029/JA080i031p04204

Butcher, N. (2005). Daily ionospheric forecasting service (DIFS) III. *Ann. Geophys.*, *23*(12), 3591–3598. https://doi.org/10.5194/angeo-23-3591-2005

Carrano, C. S., Groves, K. M., and Rino, C. L. (2019). On the relationship between the rate of change of total electron content index (ROTI), irregularity strength (C_kL), and the scintillation index (S_4). *J. Geophys. Res.: Space Phys.*, *124*(3), 2099–2112. https://doi.org/10.1029/2018JA026353

Cherniak, I., and Zakharenkova, I. (2016). First observations of super plasma bubbles in Europe. *Geophys. Res. Lett.*, *43*(21), 11137–11145. https://doi.org/10.1002/2016GL071421

Chree, C. (1913). Some phenomena of sunspots and of terrestrial magnetism at Kew Observatory. *Royal Soc.*, *212*(484-496), 75–116. https://doi.org/10.1098/rsta.1913.0003

Davies, K. (1990). *Ionospheric Radio*. London: Peter Peregrinus Ltd., https://doi.org/10.1049/PBEW031E

Davis, T. N., and Sugiura, M. (1966). Auroral electrojet activity index *AE* and its universal time variations. *J, Geophys, Res., 71*(3), 785–801. https://doi.org/10.1029/JZ071i003p00785

De La Beaujardière, O., Retterer, J. M., Pfaff, R. F., Roddy, P. A., Roth, C., Burke, W. J., Su, Y. J., Kelley, M. C., Ilma, R. R., … Cooke, D. L. (2009). C/NOFS observations of deep plasma depletions at dawn. *Geophys. Res. Lett.*, *36*(18), L00C06. https://doi.org/10.1029/2009GL038884

Doherty, P., Coster, A. J., and Murtagh, W. (2004). Space weather effects of October–November 2003. *GPS Solut., 8*(4), 267–271. https://doi.org/10.1007/s10291-004-0109-3

Dubey, S., Wahi, R., and Gwal, A. K. (2006). Ionospheric effects on GPS positioning. *Adv. Space Res.*, *38*(11), 2478–2484. https://doi.org/10.1016/j.asr.2005.07.030

Farley, D. T., Balsey, B. B., Woodman, R. F., and McClure, J. P. (1970). Equatorial spread *F*: Implications of VHF radar observations. *J. Geophys. Res.*, *75*(34), 7199–7216. https://doi.org/10.1029/ja075i034p07199

Fejer, B. G., Scherliess, L., and De Paula, E. R. (1999). Effects of the vertical plasma drift velocity on the generation and evolution of equatorial spread *F*. *J. Geophys. Res.: Space Phys.*, *104*(A9), 19859–19869. https://doi.org/10.1029/1999ja900271

Fejer, B. G., Jensen, J. W., and Su, S. Y. (2008). Seasonal and longitudinal dependence of equatorial disturbance vertical plasma drifts. *Geophys. Res. Lett.*, *35*(20), L20106. https://doi.org/10.1029/2008GL035584

Han, C. Y., Li, G. Z., Sun, W. J., Xie, H. Y., Hu, L. H., and Zhao, X. K. (2024). Generation and evolution of post-sunset equatorial plasma bubbles in East and Southeast Asia during the July 2022 geomagnetic storm. *Adv. Space Res.*, *73*(3), 1843–1853. https://doi.org/10.1016/j.asr.2023.10.046

Imtiaz, N., Younas, W., and Khan, M. (2020). Response of the low- to mid-latitude ionosphere to the geomagnetic storm of September 2017. *Ann. Geophys.*, *38*(2), 359–372. https://doi.org/10.5194/angeo-38-359-2020

Jain, A. R., Dashora, N., Sharma, S., and Pandey, R. (2010). TEC response during severe geomagnetic storms at low latitude. *Indian Journal of Radio & Space Physics*, *39*, 11–24.

Kelley, M. C. (2009). *The Earth's Ionosphere: Plasma Physics and Electrodynamics* (2nd ed). Ithaca: Elsevier.

Kikuchi, T., and Hashimoto, K. K. (2016). Transmission of the electric fields to the low latitude ionosphere in the magnetosphere-ionosphere current circuit. *Geosci. Lett.*, *3*, 4. https://doi.org/10.1186/s40562-016-0035-6

Kintner, P. M., Ledvina, B. M., and De Paula, E. R. (2007). GPS and ionospheric scintillations. *Space Weather*, *5*(9), S09003. https://doi.org/10.1029/

2006SW000260

Li, G. Z., Ning, B., Liu, L., Wan, W., and Liu, J. Y. (2009). Effect of magnetic activity on plasma bubbles over equatorial and low-latitude regions in East Asia. *Ann. Geophysi.*, *27*(1), 303–312. https://doi.org/10.5194/angeo-27-303-2009

Li, G. Z., Ning, B. Q., Wang, C., Abdu, M. A., Otsuka, Y., Yamamoto, M., Wu, J., and Chen, J. S. (2018). Storm-enhanced development of postsunset equatorial plasma bubbles around the meridian 120°E/60°W on 7–8 September 2017. *J. Geophys. Res.: Space Phys.*, *123*(9), 7985–7998. https://doi.org/10.1029/2018ja025871

Li, J. H., Ma, G. Y., Maruyama, T., and Li, Z. (2012). Mid-latitude ionospheric irregularities persisting into late morning during the magnetic storm on 19 March 2001. *J. Geophys. Res.: Space Phys.*, *117*(A8), A08304. https://doi.org/10.1029/2012JA017626

Loewe, C. A., and Prolss, G. W. (1997). Classification and mean behavior of magnetic storms. *J. Geophys. Res.: Space Phys.*, *102*(A7), 14209–14213. https://doi.org/10.1029/96JA04020

Ma, G. Y., and Maruyama, T. (2006). A super bubble detected by dense GPS network at east Asian longitudes. *Geophys. Res. Lett.*, *33*(21), L21103. https://doi.org/10.1029/2006gl027512

Manoj, C., Maus, S., Lühr, H., and Alken, P. (2008). Penetration characteristics of the interplanetary electric field to the daytime equatorial ionosphere. *J. Geophys. Res.: Space Phys.*, *113*(A12), A12310. https://doi.org/10.1029/2008JA013381

Marlia, D., Wu, F. L., Ekawati, S., Husin, A., Anggarani, S., Ednofri, N., and Yang, G. L. (2019). Analysis of ionospheric irregularities in low latitude during geomagnetic storm using GISTM network. In *IGARSS 2019-2019 IEEE International Geoscience and Remote Sensing Symposium* (pp. 7716–7719). Yokohama, Japan: IEEE. https://doi.org/10.1109/IGARSS.2019.8900326

Morton, Y. J., Yang, Z., Breitsch, B., Bourne, H., and Rino, C. (2020). Ionospheric effects, monitoring, and mitigation techniques. In Y. J. Morton, et al. (Eds.), *Position, Navigation, and Timing Technologies in the 21st Century: Integrated Satellite Navigation, Sensor Systems, and Civil Applications*. Hoboken: Wiley-IEEE Press. https://doi.org/0.1002/9781119458449.ch31

Parks, G. K. (2003). *Physics of Space Plasmas: An Introduction* (2nd ed). Oxford: Westview Press.

Putra, A. Y., Abadi, P., Kilowasid, L. O. M. M., Syafitri, N., Nuraeni, F., Wellyanita, V., Wisnu, K., Purnomo, C., Suwarno, and Rakhman, A. (2023). Investigation of geomagnetic storm effects to ionosphere over Pontianak: A study case. In *Proceedings of the International Conference on Radioscience, Equatorial Atmospheric Science and Environment and Humanosphere Science* (pp. 567–575). Indonesia: Springer. https://doi.org/10.1007/978-981-97-0740-9_51

Ram, S. T., Rao, P. V. S. R., Prasad, D. S. V. V. D., Niranjan, K., Krishna, S. G., Sridharan, R., and Ravindran, S. (2008). Local time dependent response of postsunset ESF during geomagnetic storms. *J. Geophys. Res.: Space Phys.*, *113*(A7), A07310. https://doi.org/10.1029/2007JA012922

Ram, S. T., Yokoyama, T., Otsuka, Y., Shiokawa, K., Sripathi, S., Veenadhari, B., Heelis, R., Ajith, K. K., Gowtam, V. S., … Le Huy, M. (2016). Duskside enhancement of equatorial zonal electric field response to convection electric fields during the St. Patrick's Day storm on 17 March 2015. *J. Geophys. Res.: Space Phys.*, *121*(1), 538–548. https://doi.org/10.1002/2015JA021932

Roy, B., DasGupta, A., and Paul, A. (2013). Impact of space weather events on satellite-based navigation. *Space Weather*, *11*(12), 680–686. https://doi.org/10.1002/2013SW001001

Shang, S. P., Shi, J. K., Kintner, P. M., Zhen, W. M., Luo, X. G., Wu, S. Z., and Wang, G. J. (2008). Response of Hainan GPS ionospheric scintillations to the different strong magnetic storm conditions. *Adv. Space Res.*, *41*(4), 579–586. https://doi.org/10.1016/j.asr.2007.05.020

Sori, T., Shinbori, A., Otsuka, Y., Tsugawa, T., and Nishioka, M. (2021). The occurrence feature of plasma bubbles in the equatorial to midlatitude ionosphere during geomagnetic storms using long-term GNSS-TEC data. *J. Geophys. Res.: Space Phys.*, *126*(5), e2020JA029010. https://doi.org/10.1029/2020JA029010

Spogli, L., Cesaroni, C., Di Mauro, D., Pezzopane, M., Alfonsi, L., Musicò, E., Povero, G., Pini, M., Dovis, F., … Floury, N. (2016). Formation of ionospheric irregularities over Southeast Asia during the 2015 St. Patrick's day storm. *J. Geophys. Res.: Space Phys.*, *121*(12), 12211–12233. https://doi.org/10.1002/2016JA023222

Srinivasu, V. K. D., Prasad, D. S. V. V. D., Niranjan, K., Seemala, G. K., and Venkatesh, K. (2019). L-band scintillation and TEC variations on St. Patrick's Day storm of 17 March 2015 over Indian longitudes using GPS and GLONASS observations. *J. Earth Syst. Sci.*, *128*, 69. https://doi.org/10.1007/s12040-019-1097-6

Sun, W. J., Li, G. Z., Zhang, S. R., Hu, L. H., Dai, G. F., Zhao, B. Q., Otsuka, Y., Zhao, X. K., Xie, H. Y., … Perwitasari, S. (2024a). Regional ionospheric super bubble induced by significant upward plasma drift during the 1 December 2023 geomagnetic storm. *J. Geophys. Res.: Space Phys.*, *129*(6), e2024JA032430. https://doi.org/10.1029/2024JA032430

Sun, W. J., Li, G. Z., Zhao, B. Q., Zhang, S. R., Otsuka, Y., Hu, L. H., Dai, G. F., Zhao, X. K., Xie, H. Y., … Perwitasari, S. (2024b). Midlatitude plasma blob-like structures along with super equatorial plasma bubbles during the May 2024 great geomagnetic storm. *Geophys. Res. Lett.*, *51*(21), e2024GL111638. https://doi.org/10.1029/2024GL111638

Tsurutani, B. T., Verkhoglyadova, O. P., Mannucci, A. J., Saito, A., Araki, T., Yumoto, K., Tsuda, T., Abdu, M. A., Sobral, J. H. A., … Vasyliunas, V. M. (2008). Prompt penetration electric fields (PPEFs) and their ionospheric effects during the great magnetic storm of 30–31 October 2003. *J. Geophys. Res.: Space Phys.*, *113*(A5), A05311. https://doi.org/10.1029/2007JA012879

Weygand, J. M., Zesta, E., and Troshichev, O. (2014). Auroral electrojet indices in the Northern and Southern Hemispheres: A statistical comparison. *J. Geophys. Res.: Space Phys.*, *119*(6), 4819–4840. https://doi.org/10.1002/2013JA019377

World Data Center for Geomagnetism, Kyoto, M. Nose, T. Iyemori, M. Sugiura, T. Kamei (2015a). Geomagnetic AE index. https://doi.org/10.17593/15031-54800.

World Data Center for Geomagnetism, Kyoto, M. Nose, T. Iyemori, M. Sugiura, T. Kamei (2015b). Geomagnetic Dst index. https://doi.org/10.17593/14515-74000.

World Data Center for Geomagnetism, Kyoto, S. Imajo, A. Matsuoka, H. Toh, and T. Iyemori (2022). Mid-latitude Geomagnetic Indices ASY and SYM (ASY/SYM Indices). https://doi.org/10.14989/267216.

Yeh, K. C., and Liu, C. H. (1982). Radio wave scintillations in the ionosphere. *Proc. IEEE*, *70*(4), 324–360. https://doi.org/10.1109/PROC.1982.12313